RESEARCH ARTICLE

ROBOTIC MATERIALS

Design and printing of proprioceptive three-dimensional architected robotic metamaterials

Huachen Cui[1], Desheng Yao[1], Ryan Hensleigh[1], Haotian Lu[2], Ariel Calderon[1], Zhenpeng Xu[1], Sheyda Davaria[3], Zhen Wang[1], Patrick Mercier[4], Pablo Tarazaga[5], Xiaoyu (Rayne) Zheng[1,2,3,6]*

Advances in additive manufacturing techniques have enabled the creation of stimuli-responsive materials with designed three-dimensional (3D) architectures. Unlike biological systems in which functions such as sensing, actuation, and control are closely integrated, few architected materials have comparable system complexity. We report a design and manufacturing route to create a class of robotic metamaterials capable of motion with multiple degrees of freedom, amplification of strain in a prescribed direction in response to an electric field (and vice versa), and thus, programmed motions with self-sensing and feedback control. These robotic metamaterials consist of networks of piezoelectric, conductive, and structural elements interwoven into a designed 3D lattice. The resulting architected materials function as proprioceptive microrobots that actively sense and move.

Advances in additive manufacturing techniques have enabled the fabrication of materials with ultrahigh stiffness (*1*) and damage tolerance (*2*, *3*), exotic mechanical behaviors (*4*, *5*), negative thermal expansion coefficients (*6*), fluid control (*7*), and wave transmissions (*8*). These materials can be digitally designed by placing structural elements as bits and atoms in a three-dimensional (3D) layout. The potential of architecting electronic and multifunctional materials and their combinations is still elusive, as most additive fabrication techniques have focused on single structural materials such as polymers, metals, and ceramics. Architecting functional materials could offer exotic and configurable properties in functional space, such as directional sensing (*9*), morphing (*10*), and reconfigurability (*11*, *12*).

Piezoelectric materials, which are capable of converting an electrical field into mechanical strain and vice versa (*13*), are ideal candidates for providing both sensing and actuation functions in a robotic system. These materials are widely employed in precision actuators (*14*), manipulators (*15*), accelerometers (*16*), and tactile sensors (*17*, *18*) to generate robotic motions and sensing feedback. However, their electric field–induced strain, as a result of asymmetric displacement of ions in crystal dimensions, is derived from and thus limited

by the naturally existing crystal structures, leading to a magnitude of <0.5% [i.e., the strain range in lead zirconate titanate (PZT) ceramic and single-crystalline lead magnesium niobate–lead titanate (PMN-PT) is <0.1 and <0.5%, respectively] in only the normal and shear directions (*13*). To use piezoelectric materials as transducers in robotic systems, the manufacturing process must involve extensive processing and assembly steps—such as ceramic machining (*19*), lamination (*20*), attaching planar electrodes for both activation and driving (*21*), and integration with transmission mechanisms (*22*)—to amplify the piezoelectric strain and transform the strain into motion in desired directions. These manufacturing routes usually process solid piezoelectric materials only and cannot precisely pattern electrodes, making it difficult to reduce the weight of an actuation element and activate bidirectional piezoelectric effects at small scales (*23*).

We show that a two-way conversion from an electric field to an arbitrary mechanical strain in a prescribed direction (and vice versa) can be achieved via a 3D network of interconnected piezoactive, conductive, and structural phases (Fig. 1A). Through analytical, numerical, and experimental validations, we show that these 3D microarchitected piezoelectric materials exhibit piezoelectric strain constants that cannot be achieved in standard materials and result in a wealth of electric field–induced strain conversions—including tension, shear, twisting, and flexure degrees of freedom (DoFs) and their combinations—as well as amplification of strain and logic-related subtraction and addition of strains. We developed a charge-programmed multimaterial additive manufacturing technique capable of directly assembling conductive, piezoactive, and structural mate-

rials into a complex 3D microarchitecture, which leads to a class of robotic metamaterials. We use the term "robotic metamaterials" to represent materials with designed 3D microarchitectures that directly serve as microrobots capable of performing many robotic tasks, including locomotion, steering, stepping, and two-way sound and ultrasonic transductions, as well as decision-making via feedback control (*24*).

Rational design of robotic metamaterials with arbitrary strain modes

The core concept of architected materials is the unrestricted placement of materials in a 3D cellular topology that either bypasses limitations inherent in natural crystals or mimics them to achieve desired properties. We introduce a convenient and robust strategy to architect piezoactive, conductive, and structural phases (Fig. 1A) in 3D space. Such multimaterial metamaterials are capable of receiving an input electric field and outputting a desired mode of strain that includes DoFs beyond the Cauchy strain components (normal and shear strains) (*25*), such as normal, shear, twisting, and flexure modes as well as their combinations and amplifications.

Because the existing piezoelectric tensors are not sufficient to describe all DoFs, we define the generalized piezoelectric tensors d_{nm} and $\bar{d}_{nm}$ on the basis of Cosserat solids (*26*) to describe the strain conversions of the architected piezoelectric materials (Fig. 1B)

$$\varepsilon_m = d_{nm}E_n; \quad \varphi_m = \bar{d}_{nm}E_n \qquad (1)$$

where E_n is the electric field along the n direction in Cartesian coordinates (n = 1 to 3); ε_m and φ_m (m = 1 to 6) are the directional strain and coupled strain tensors (*25*), respectively; d_{nm} is the piezoelectric tensor that describes only the correlation between the normal or shear strain and the electric field; and $\bar{d}_{nm}$ is the extended piezoelectric tensor with components that denote the additional strain modes, including twist and flexure.

To design a piezoelectric microarchitecture that displays a desired global strain mode d_{nm} (or $\bar{d}_{nm}$) (Fig. 1B; see movie S1 for 36 distinguished strain modes), we start by identifying the motion of a stack of virtual characteristic planes within a unit cell of the microarchitecture (Fig. 1, C and D) and the local strain of the piezoactive struts that make up the unit cell (Fig. 1E and movie S1). The virtual characteristic planes can be considered "pinned" by the piezoactive struts to allow unconstrained motion and display a motion representing the desired global strain. As shown in fig. S1, A to D, the characteristic planes undergo distance changes, slip, rotation, and tilt corresponding to strain modes such as normal strain (ε_m, with m = 1 to 3), shear (ε_m, with m = 4 to 6),

[1]Department of Civil and Environmental Engineering, University of California, Los Angeles, CA 90095, USA. [2]Department of Mechanical and Aerospace Engineering, University of California, Los Angeles, CA 90095, USA. [3]Department of Mechanical Engineering, Virginia Tech, Blacksburg, VA 24061, USA. [4]Department of Electrical and Computer Engineering, University of California, San Diego, CA 92093, USA. [5]Department of Mechanical Engineering, Texas A&M University, College Station, TX 77843, USA. [6]California NanoSystems Institute, University of California, Los Angeles, CA 90095, USA.
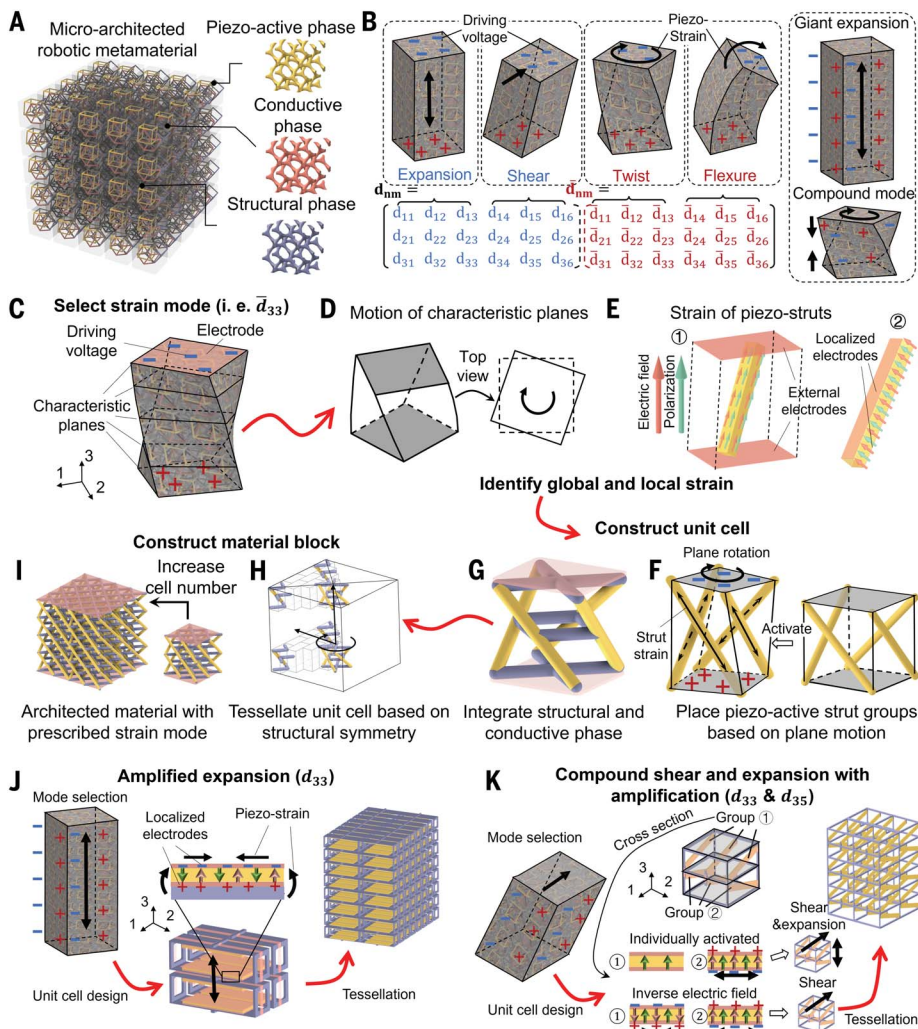*Corresponding author: Email: rayne@seas.ucla.edu

Fig. 1. Rational designs of robotic metamaterials with arbitrary strain modes. (**A**) Schematic of the piezoelectric metamaterial consisting of piezoactive, conductive, and structural phases. (**B**) Schematic of various strain modes and a piezoelectric strain matrix with extended tensors (red), enabled by metamaterial design and compared with the 18 tensors in natural piezoelectric ceramics (blue). (**C** to **I**) Schematic of the design rationale for the piezoelectric metamaterials. The example shown here is for the $\bar{d}_{33}$ (twisting) mode. (**J**) Designs of a piezoelectric robotic metamaterial with amplified expansion. (**K**) Schematic of the compound and decoupled expansion-shear mode with strain amplification. ①, external electrodes; ②, localized electrodes.

tural phase and a conductive phase (Fig. 1G) in a layout that matches the symmetry of the piezoactive struts (see materials and methods for details on different phases).

In the last step, we tessellate the unit cells into a "metacrystal" that reflects the effective response of the unit cell (see materials and methods and fig. S1, I to L, for the choice of tessellation orientations). For example, to generate a twisting metamaterial, we tessellate the unit cell in cylindrical coordinates along the radial (r), angular (θ), and height (z) directions (Fig. 1, H and I, and movie S1). This aperiodic tessellation is scalable to an infinite number of unit cells and bypasses the effect of the number of unit cells when tessellated in Cartesian coordinates, for which the twist strain would vanish when reduced to a Cauchy continuum as the unit cell number increases (27) (fig. S2). As such, these metamaterial concepts are scalable, and the coefficient is invariant of the number of unit cells in all directions. Designs with all strain modes shown in the extended matrix are summarized in table S1.

The interpenetrating piezoactive, structural, and conductive phases allow amplification and logic-related subtraction and addition of strains, leading to the coupling and suppression of selected strain modes. Figure 1J shows the unit cell design featuring amplified expansion by tessellating pairs of piezoactive and structural struts (28). Figure 1K demonstrates the design with localized electrodes. The localized electrode architecture that covers selected groups of struts allows for programming of the polarization and electric field direction within the unit cell (Fig. 1K; see fig. S3 for polarization and driving voltage programming), thereby achieving a compound strain mode with both shear and expansion strain output or a decoupled strain mode with doubled shear strain and suppressed expansion.

We implemented a computational framework that predicts and verifies the piezoelectric coefficients—d_{nm} and $\bar{d}_{nm}$, respectively—of the metacrystal designs. This is achieved by calculating the total induced-load contribution of the connected piezoactive struts within the cubic volume under an electric field [materials and methods and supplementary text section 1 (SM 1)]. SM 2 and fig. S4 show the finite element analysis results that verify the actuation modes.

Additive manufacturing of robotic metamaterials

We developed a charge-programmed multi-material additive manufacturing technique capable of assembling piezoactive, structural, and conducting phases into a complex 3D microarchitecture. First, a negatively charged resin [which can be selectively deposited with metals (29)] and a highly loaded nanoparticle
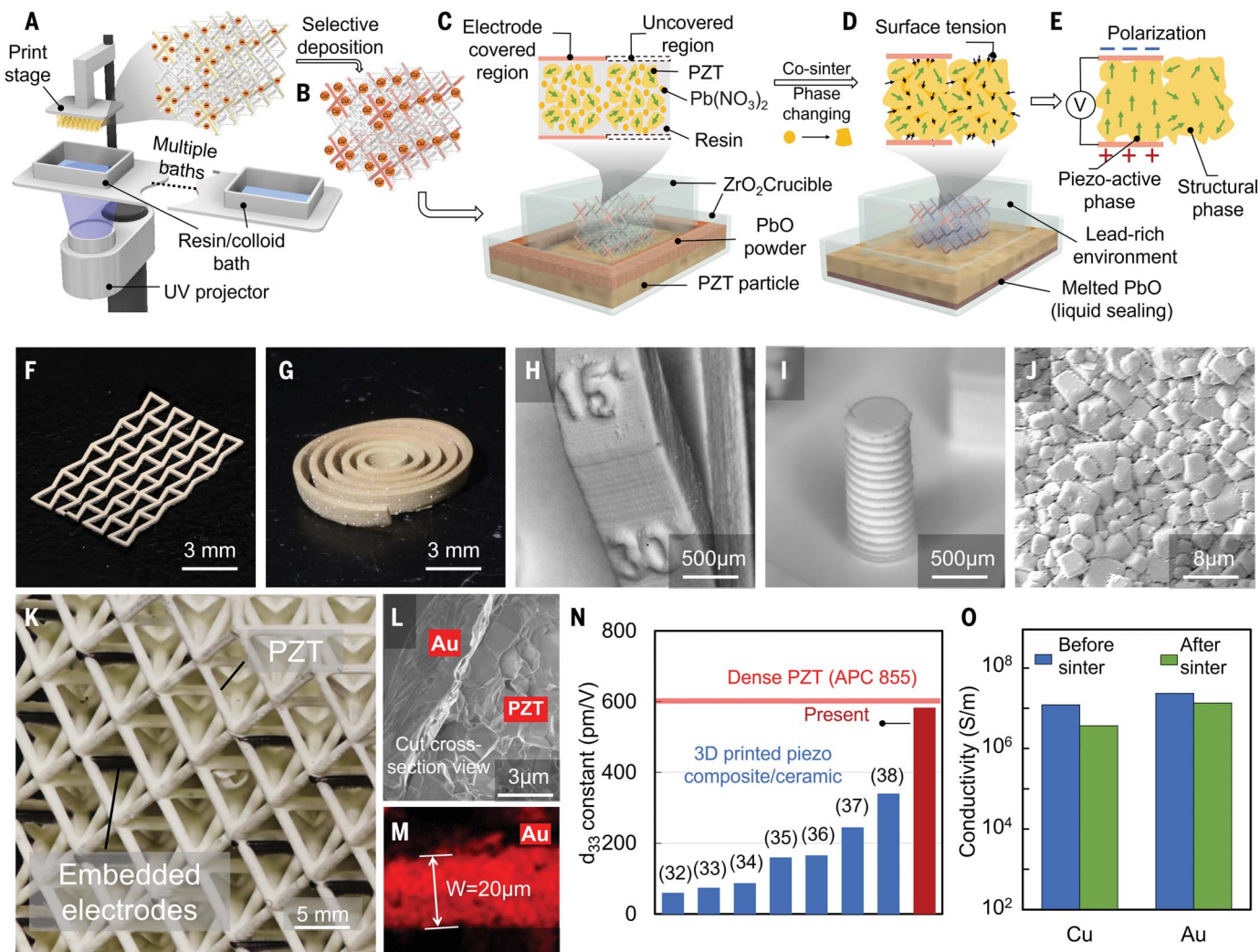
twist (φ_m, with m = 1 to 3), and flexure (φ_m, with m = 4 to 6). Figure 1D shows an example of a cube that twists upon application of an electric field in the direction of the 3-axis ($\bar{d}_{33}$ mode), which is represented by the in-plane rotation of the characteristic planes (Fig. 1D). The local strain of a piezoactive strut within the unit cell, either expanding or contracting, is determined by the direction of the strut, polarization, and electric field (see materials and methods for details on local strain identification). The electric field is generated by a conducting phase that either covers the sides of the lattice topology [external electrodes (Fig. 1E, ①)] or penetrates the topology [localized electrodes (Fig. 1E, ②)], covering both sides of the active struts and resulting in a

shorter distance between electrodes and a stronger electric field.

The next design step is to place the piezoactive struts in a spatial layout such that their local strain drives the virtual characteristic planes to display the motion path corresponding to the target global strain mode (d_{nm} or $\bar{d}_{nm}$) (movie S1). Figure 1F presents the design of the piezoactive struts that generate a clockwise rotation of the characteristic planes, resulting in a twist strain mode and corresponding to a nonzero piezoelectric twist coefficient, $\bar{d}_{33}$. The 3D microarchitectural layouts of piezoactive struts for other strain modes (including expansion, shear, and flexure) are summarized in fig. S1, E to H. The full unit cell design is then completed by adding a struc-

Fig. 2. Multimaterial fabrication platform. (**A** and **B**) Schematic illustrations of the charge-programmed multimaterial additive fabrication of 3D piezoelectric ceramics with embedded electrodes. UV, ultraviolet. (**C** and **D**) Schematics of the sintering process of highly loaded piezoelectric ceramics with localized electrodes. (**E**) Schematic of the selective activation (polarization) process of the piezoactive phase. (**F** to **I**) Optical images of as-fabricated samples. (**J**) Scanning electron microscopy (SEM) image of the cross section of the sintered PZT. (**K**) Optical image of a printed piezoelectric metamaterial block with embedded 3D electrodes. (**L**) SEM image of the boundary between the PZT and Au electrode. (**M**) Elemental mapping of a selectively deposited thin wire, showing the minimum deposition width (W). (**N**) Comparison of piezoelectric charge coefficients between piezoceramics presented in this study and current 3D-printed piezoelectric materials (*32–38*). (**O**) Conductivity of Cu and Au conductive phases before and after sintering.

colloid were printed via the multimaterial 3D printing system (materials and methods), as shown in Fig. 2A. The nanoparticle colloid consists of 15 to 50 vol % PZT (APC 855), featuring a high piezoelectric strain constant (d_{33} = 600 pm/V) and 5 to 15% lead nitrate, which is used as a liquid-phase–sintering agent (*30*). The conductive phase was then selectively deposited onto the charged resins, forming a 3D microarchitecture with electrodes (Fig. 2B and materials and methods). The deposited architectures were cosintered with an optimized temperature profile in a gas environment (fig. S5) to prevent degradation of the piezoelectricity of the piezoceramics and conductivity of the electrodes (Fig. 2C). Additionally, lead oxide was used to provide a liquid seal and lead-rich environment to suppress lead evaporation of PZT at temperatures higher than 800°C (Fig. 2D and SM 3). The lead nitrate particles within the printed architecture melted and induced contraction of the PZT particles as a result of their surface tension, which densified the PZT and reduced the porosity. Next, the architected piezoceramics were polarized by applying a strong electric field through the deposited metals at an elevated temperature (SM 3 and fig. S5). After polarization, the regions not covered with electrodes remained inactive (unpolarized) and were employed as the structural phase (Fig. 2E). Other ceramics, such as silicon oxy-carbide (SiOC) (*31*), could also be employed as the structural phase to enhance the stiffness of the metamaterial.

This 3D fabrication approach allows the fabrication of piezoactive materials with precise, microscale 3D architectures and low porosity (Fig. 2, F to H). Figure 2K shows a robotic metamaterial block with embedded electrodes. The gapless bonding between the piezoactive and conductive phases (Fig. 2L) results in minimal dielectric loss when an electric field is applied. The minimum achievable feature size of the conductive phase reaches 20 μm (Fig. 2M), ensuring precise control of the localized electric field when voltages are applied through these conductive phases. The

as-printed piezoelectric solids reach a measured piezoelectric constant (d_{33}) as high as 583 pm/V (measured with a d33 meter, APC 90-2030), indicating that these materials outperform existing 3D printable piezoelectric composites or ceramics (Fig. 2N) (32–38). The selectively patterned conductive phases are highly conductive (SM 4), achieving values of 3.7×10^6 and 1.35×10^7 S/m (where 1 S = 1 A/V) after sintering for Cu and Au, respectively (Fig. 2O), which makes them suitable for subsequent actuation with negligible energy loss. The surface texture and roughness of differ-

ent materials of the as-fabricated samples are summarized in SM 6 and fig. S7. See SM 5 and fig. S6 for the characterization of mechanical properties of the as-printed lattice materials, including strength, elastic modulus, and durability. The high-precision fabrication, highly responsive 3D-printed PZT, and highly conductive deposited metals enable the implementation of metamaterial designs.

Multi-DoF amplified and programmed strain

To verify the designed strain modes of the robotic metamaterials, we measured the electric

field–activated deformation of the as-fabricated and polarized samples via high-precision full-field scanning laser Doppler vibrometry (Polytec, PSV-500) (Fig. 3A). A sinusoidal sweep signal with 50-V amplitude was applied through the layered external electrodes, whereas the activated deformation was measured by tracing the side surface of the metamaterial (Fig. 3A) and reconstructed as operational deflectional shapes in the quasi-static region for visualization. Figure 3, B and C, displays an optical image of a twist ($\bar{d}_{33}$) mode lattice with external electrodes and its side-surface deformation,
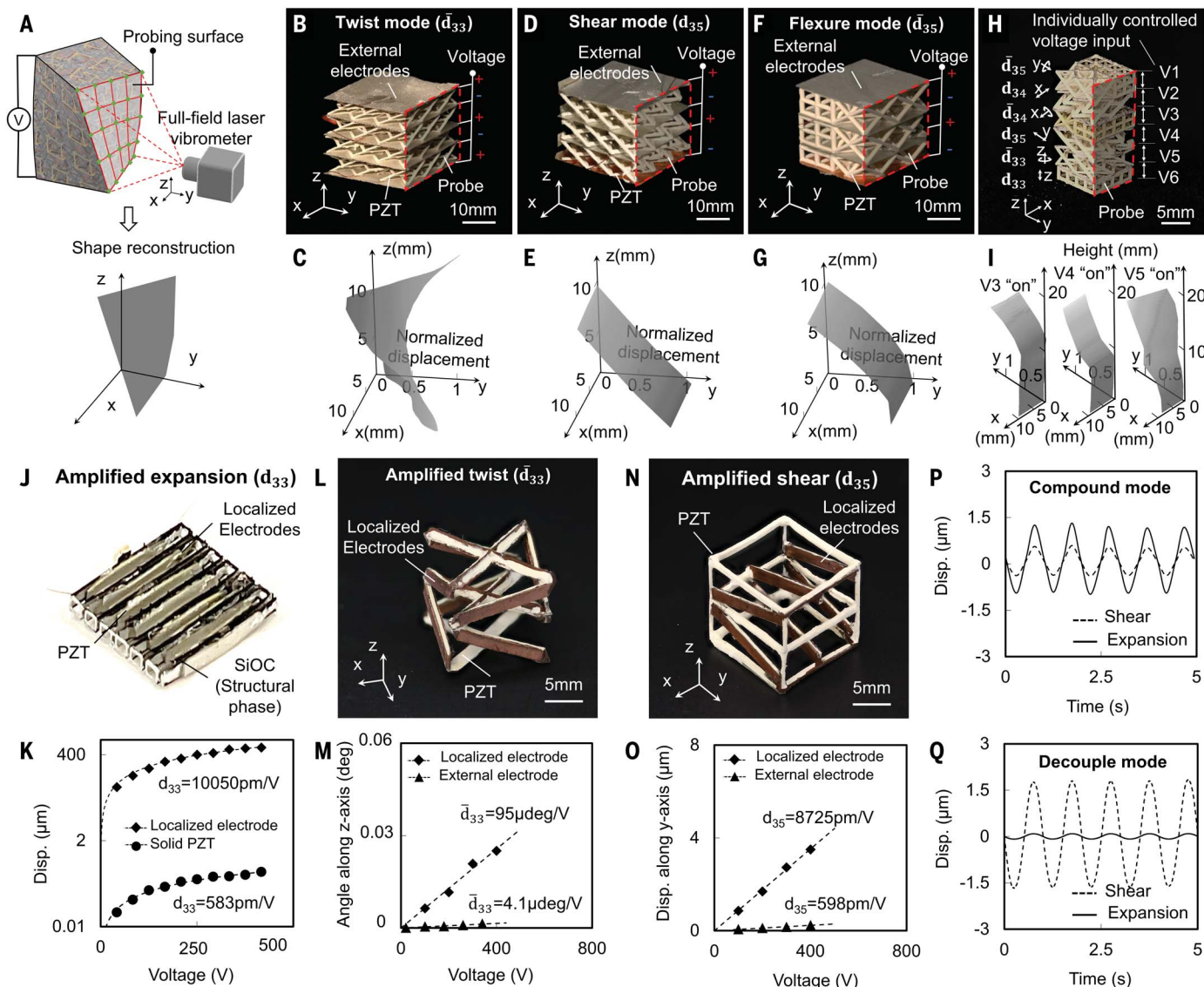

Fig. 3. Experimental verification of robotic metamaterial designs. (**A**) Schematic of the test setup with a laser vibrometer to measure the deformation of the side surface of the lattice. (**B** to **G**) Optical images of the twist, shear, and flexure mode lattice and their side-surface deformation. (**H**) Optical image of a modularized piezoelectric actuator with six DoFs. (**I**) Deformation of the side surface of the 6-DoF piezoelectric actuator working in three representative operating modes (d_{34}, d_{35}, and $\bar{d}_{33}$ modes). (**J**) Optical image of a piezoelectric metamaterial with amplified expansion. (**K**) Displacement of the metamaterial

with localized electrodes and solid PZT material with external electrodes as a function of the input voltage. (**L**) Optical image of the piezoelectric metamaterial with amplified twist and suppressed expansion. (**M**) Twist angle of the metamaterial with external and localized electrodes as a function of input voltage. (**N**) Optical image of the piezoelectric metamaterial with amplified shear. (**O**) Shear displacement of the metamaterial with external electrodes and localized electrodes as a function of input voltage. (**P** and **Q**) Displacement of compound and decoupled expansion-shear modes with sinusoidal voltage input.

showing a wrapped shape that corresponds to a twisted solid (Fig. 1C). Operational deflectional shapes for shear (d_{34}) and flexure ($\bar{d}_{35}$) mode lattices are summarized in Fig. 3, D and E, and Fig. 3, F and G, respectively. Different strain modes can be combined into a single-element piezoelectric lattice to achieve a multi-DoF metamaterial actuator with six individually actuatable architecture designs with six DoFs, including the d_{33}, d_{34}, d_{35}, $\bar{d}_{33}$, $\bar{d}_{34}$, and $\bar{d}_{35}$ modes (Fig. 3, H and I, and movie S2). This multi-DoF actuator has a density of 0.88/cm^3, which is an order of magnitude lower than that of existing piezoactuators with dense PZT (23) (fig. S8). We demonstrate a high-speed galvanometer actuated by two multi-DoF actuators assembled with two reflective mirrors (movie S3). Figure S9 shows a star pattern drawn by the guided laser beam (10 cycles at 20 Hz, root mean square precision of $50 \pm 13\,\mu$m). This is achieved by programming the input voltage that controls the tilt angle of the metamaterial (see SM 7 for details of the laser pattern reconstruction).

We fabricated microarchitectures with embedded electrodes and demonstrated strain amplification, strain compounding, and strain addition and subtraction enabled by the localized electrodes and microarchitecture design. Figure 3, J, L, and N, present as-fabricated lattices with localized electrodes that feature amplified expansion (d_{33}; Fig. 1J), amplified twist ($\bar{d}_{33}$; fig. S3), and amplified shear (d_{34}; Fig. 1K), respectively. The displacement versus the driving voltage of the lattices was measured by the laser vibrometer and plotted (Fig. 3, K, M, and O) to derive the corresponding strain coefficients. Compared with the strain coefficients of lattices with layered external electrodes, the piezoelectric coefficients of the localized electrodes (i.e., d_{33} = 10,050 pm/V) are amplified, with values two orders of magnitude higher than that of their native material (583 pm/V). The compound expansion-shear strain and the decoupled pure shear strain are demonstrated, using designs from Fig. 1K, by programming the local polarization and driving electric field within the embedded electrode architectures (Fig. 3, P and Q).

Robotic metamaterials as proprioceptive microrobots

These piezoceramic architectures have bidirectional electrical-to-mechanical energy conversion—namely, direct and inverse piezoelectric effects. These metamaterials can be exploited as a proprioceptive microrobotic system with feedback control and without the need to combine transmissions and external sensors. Within a single piece of piezoelectric architecture, selected regions serve as actuation limbs using the inverse piezoelectric effect, whereas other regions that use the direct and bidirectional piezoelectric effects serve as strain

sensors and pulse-echo elements, respectively (Fig. 4A).

We fabricated one piece of metamaterial with an amplified d_{33} mode (Fig. 1J) as a multimodal microrobot (Fig. 4B; see SM 8 and figs. S10 and S11 for an alternative version consisting of compound flexure-twist mode lattices). Selected regions serve as robotic limbs capable of actuation and load carrying, with the ability to sense both contact forces and remote objects. The microrobot is controlled by a closed-loop system via its sensing components (fig. S12). The microrobot consists of three individually actuatable regions that serve as its body, rear legs, and front legs (Fig. 4B). The coordinated motion of these three regions enables three distinguishable modes described as walking, turning, and jumping (Fig. 4B; see materials and methods and fig. S14, A and B, for motion planning based on the three limbs). The 3D localized electrode interconnects all piezoactive elements within one region and minimizes the number of connection leads, enabling a compact design (without additional circuit boards or leads wired to individual piezoactive elements) and making the microrobot lightweight (740 mg).

In contrast to existing piezoelectric actuation mechanisms in which leveraging or transmission methods are employed to amplify displacement at the cost of reducing blocking force, a feature of the actuation performance of the robotic metamaterial is its simultaneously increased blocking force and displacement via its skeletal actuator layout. An actuator connected with a transmission system for robotic motions typically leads to a trade-off between blocking force and step length, owing to the compliant levering mechanism involved (39, 40). We show that these architected piezoelectric robotic limbs (Fig. 4A), composed of a network of microscale actuation units distributed throughout the robot body in a fashion similar to skeletal muscles, breaks this trade-off and simultaneously produce long steps and high blocking force with high system stiffness. A comparison between the skeletal actuation architecture and actuator-transmission mechanism is described in fig. S13 and SM 9. Although a transmission system effectively amplifies the displacement, its additional levering inevitably reduces the system stiffness and therefore the blocking force (Fig. 4C; N denotes the number of unit cells of the metamaterial block), resulting in a decreased payload capability of the robot when driven at higher speeds. The interconnected microactuator and embedded electrode microarchitecture allow the driving voltage to be applied locally at each element, enabling a higher driving electric field and thus an amplified displacement. This is achieved while maintaining the overall stiffness through the interconnections of the unit cells without compliant transmissions. These

features enhance the performance of the microrobot, including high speed, payload, and resonance.

The long steps and high resonance of the metamaterial limb enable a maximum speed of 128 mm/s in the walking mode and a turning rate of 90°/s (Fig. 4D and movie S4; see fig. S14 for the frequency response of the limb and speed benchmark). With its broadband response (fig. S14), the robotic metamaterial achieves a short rise time to impulse voltage inputs (41). This enables the release of actuation energy within 1 ms, resulting in the microrobot lifting its front legs into the air and then lifting its body and rear legs, thus allowing it to step up from the ground (movie S4). The jumping mode enables the microrobot to climb over elevated and rough surfaces (Fig. 4E and movie S4), movement that is not achievable by piezoelectric microrobots with small strokes (42, 43). The stiffness of the piezoelectric metamaterial elements enables a large system payload. Various weights (1 to 5.6 g) are loaded on the microrobot, and its speed is measured by digital image correlation. More than 80% of the original speed is retained for a 500% payload, compared with a >80% speed reduction with a <200% payload for microrobotic systems using a compliant mechanism (Fig. 4F) (39, 44).

By assigning sections of the piezoactive phases as the sensing element and using its direct piezoelectric effects via 3D embedded electrodes, we demonstrate that the robotic metamaterial is capable of self-sensing its strain change and responding to external stimuli, which allows closed-loop control and quick reactions to external stimuli. As shown in Fig. 4B, the selectively deposited electrodes separate a strain-sensing section from a piezoactive element with a 100-μm isolation gap, which eliminates electrical coupling. This section is integrated with a microcontroller to form a closed-loop control system that receives the sensing voltage and sends the control voltage to the actuation regions. The self-sensing voltage signal updates as the actuator element deforms, allowing real-time monitoring of the gait status and response to stimuli (see fig. S12 for control loop design; see SM 10 and fig. S15 for more details on proprioception and exteroception). Figure 4G demonstrates the gait-monitoring signal, detection of the external impact, and programmed reaction within 0.1 ms upon a drop-weight impact during locomotion (SM 11). Movie S5 shows other programmed reactions that include stopping or turning upon detecting an obstacle. The high payload of the metamaterial-enabled robot allows for the integration of an onboard power (7.4 V), a driver, and a microcontroller, paving the way for fully untethered operations with closed-loop control (SM 12, fig. S16, and movies S6 and S7).
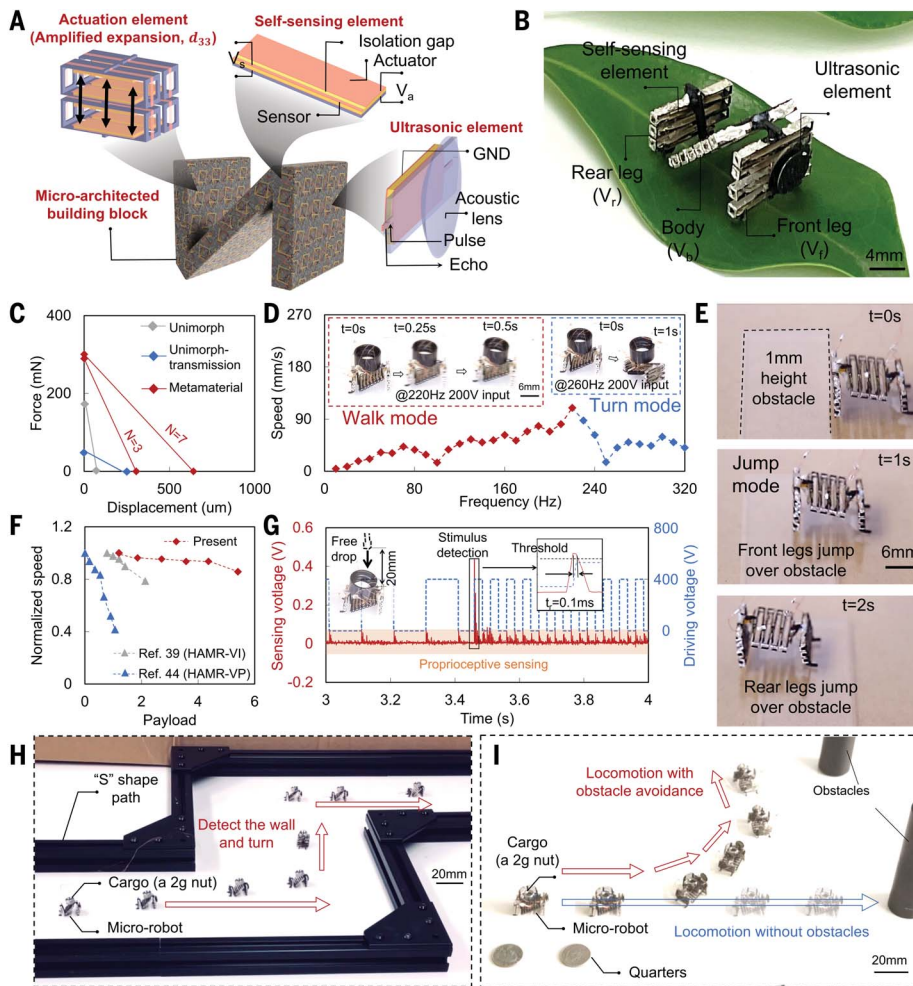
Fig. 4. Stimuli-responsive multimodal mobile microrobot. (**A**) Schematic of the microarchitected piezoelectric metamaterial building block with an embedded actuation element, an embedded self-sensing element, and a contactless detection element. GND, ground. (**B**) Optical image of the mobile robot. (**C**) Working curves of a unimorph, a unimorph assembled with a transmission mechanism, and the fabricated piezoactuator with multiple unit cells. N, number of unit cells of the metamaterial block. (**D**) Speed as a function of stepping frequency. (**E**) Optical image of the microrobot climbing over a 1-mm-high obstacle in jumping mode. (**F**) Normalized speed of the microrobot under various payload conditions. HAMR-VI and HAMR-VP denote two versions of the Harvard Ambulatory Microrobot. (**G**) Sensing voltage and mobile voltage as a function of time during the impact test. (Inset) Optical image of the drop-weight impact test of the microrobot with a basket. (**H**) Trajectory of the microrobot navigating an S-shaped path. (**I**) Trajectory of the microrobot with and without obstacle.

The robotic metamaterial is also capable of sensing and reacting to noncontact stimuli when the pulse-echo element functions with bidirectional piezoelectric effects. As shown in Fig. 4B, an element on a frontal leg is capable of emitting and receiving focused ultrasonic waves with a semispherical acoustic lens printed with the structural phase. The echo signal (fig. S17 and materials and methods) from the remote object is processed by the closed-loop control system that updates the driving voltage to navigate through an S-shaped path and avoid remote obstacles (Fig. 4, H and I, and movie S8).

Discussion and outlook

We introduced a strategy to design and construct a class of robotic metamaterials that incorporate electronic, structural, and conducting microscale strut elements in a 3D architecture. These multifunctional metamaterials revealed a myriad of strain modes, including twisting, flexure, compound, decoupled, and amplified strains. The microarchitecture designs surpass the limitations of natural piezoelectric crystals in which the piezoelectric strain relies on the available natural crystalline structures. The design strategy can be combined with a topology-optimization algorithm to generate arbitrary piezoelectric tensors.

The multimaterial additive manufacturing technique reported herein combines piezoceramic, metallic, and structural materials into a complex 3D architecture. The resulting metamaterial blocks with milli- to centimeter dimensions are capable of outputting multi-DoF motions with high blocking force as well as sensing contact and remote stimuli. This is accomplished without any external sensors and transmissions. Compared with other actuation materials (e.g., dielectric elastomers), the robotic metamaterials have low driving voltage, broad frequency range, two-way sensing, and actuation. The reported design framework and manufacturing methods have direct implications for the future development of miniaturized robots, transducers, and robotic materials; it will be possible to achieve desired motions and decision-making via simplified artificial materials.

REFERENCES AND NOTES

1. X. Zheng *et al.*, *Science* **344**, 1373–1377 (2014).
2. A. J. D. Shaikeea, H. Cui, M. O'Masta, X. R. Zheng, V. S. Deshpande, *Nat. Mater.* **21**, 297–304 (2022).
3. M.-S. Pham, C. Liu, I. Todd, J. Lertthanasarn, *Nature* **565**, 305–311 (2019).
4. X. Zheng *et al.*, *Nat. Mater.* **15**, 1100–1106 (2016).
5. Y. Kim, H. Yuk, R. Zhao, S. A. Chester, X. Zhao, *Nature* **558**, 274–279 (2018).
6. H. Xu, D. Pasini, *Sci. Rep.* **6**, 34924 (2016).
7. N. A. Dudukovic *et al.*, *Nature* **595**, 58–65 (2021).
8. N. J. Gerard *et al.*, *Appl. Phys. Lett.* **114**, 231902 (2019).
9. H. Cui *et al.*, *Nat. Mater.* **18**, 234–241 (2019).
10. K. Liu, F. Hacker, C. Daraio, *Sci. Robot.* **6**, eabf5116 (2021).
11. J. T. B. Overvelde *et al.*, *Nat. Commun.* **7**, 10929 (2016).
12. J. T. B. Overvelde, J. C. Weaver, C. Hoberman, K. Bertoldi, *Nature* **541**, 347–352 (2017).
13. S. Trolier-McKinstry, S. Zhang, A. J. Bell, X. Tan, *Annu. Rev. Mater. Res.* **48**, 191–217 (2018).
14. Z. Li *et al.*, *Adv. Sci.* **7**, 2001155 (2020).
15. H. Götze, L. Pagel, *Microelectron. Eng.* **84**, 1333–1336 (2007).
16. P. Scheeper, J. O. Gulløv, L. M. Kofoed, *J. Micromech. Microeng.* **6**, 131–133 (1996).
17. P. Zhu *et al.*, *Adv. Energy Mater.* **10**, 2001945 (2020).
18. M. Han *et al.*, *Nat. Electron.* **2**, 26–35 (2019).
19. H. Kiso, T. Taguchi, M. Fukuhara, T. Kimura, *Bull. Jpn. Soc. Precis. Eng.* **21**, 142–143 (1987).
20. M. F. M. Sabri, T. Ono, S. M. Said, Y. Kawai, M. Esashi, *J. Microelectromech. Syst.* **24**, 80–90 (2015).
21. Y. P. Singh, V. K. Jain, P. Kumar, D. C. Agrawal, *J. Mater. Process. Technol.* **58**, 24–31 (1996).
22. Y. Chen, N. Doshi, B. Goldberg, H. Wang, R. J. Wood, *Nat. Commun.* **9**, 2495 (2018).
23. Z. Li *et al.*, *Adv. Mater.* **34**, e2107236 (2022).
24. M. A. McEvoy, N. Correll, *Science* **347**, 1261689 (2015).
25. A. C. Eringen, *Microcontinuum Field Theories: I. Foundations and Solids* (Springer, 1999); https://www.springer.com/gp/book/9780387986203.
26. E. M. P. Cosserat, F. Cosserat, *Theory of Deformable Bodies* (NASA, 1970).

27. T. Frenzel, M. Kadic, M. Wegener, *Science* **358**, 1072–1074 (2017).
28. B. Rodriguez, H. Kalathur, R. Lakes, *Phys. Stat. Sol. B* **251**, 349–353 (2014).
29. R. Hensleigh *et al.*, *Nat. Electron.* **3**, 216–224 (2020).
30. R. M. German, P. Suri, S. J. Park, *J. Mater. Sci.* **44**, 1–39 (2009).
31. H. Cui, R. Hensleigh, H. Chen, X. Zheng, *J. Mater. Res.* **33**, 360–371 (2018).
32. Y. Zeng *et al.*, *Micromachines* **11**, 713 (2020).
33. S. M. Gaytan *et al.*, *Ceram. Int.* **41**, 6610–6619 (2015).
34. X. Song *et al.*, *Rapid Prototyping J.* **23**, 44–53 (2017).
35. Z. Chen *et al.*, *Nano Energy* **27**, 78–86 (2016).
36. J. Cheng, Y. Chen, J.-W. Wu, X.-R. Ji, S.-H. Wu, *Sensors* **19**, 4078 (2019).
37. H. Chabok *et al.*, in *Proceedings of the ASME/ISCIE 2012 International Symposium on Flexible Automation* (American Society of Mechanical Engineers, 2013), pp. 433–444.
38. Y.-Z. Ji *et al.*, *Adv. Eng. Mater.* **19**, 1600803 (2017).
39. N. Doshi *et al.*, in *2015 IEEE/RSJ International Conference on Intelligent Robots and Systems (IROS)* (IEEE, 2015), pp. 4119–4126.
40. K. Jayaram, J. Shum, S. Castellanos, E. F. Helbling, R. J. Wood, in *2020 IEEE International Conference on Robotics and Automation (ICRA)* (IEEE, 2020), pp. 10305–10311.
41. S. J. Rupitsch, *Piezoelectric Sensors and Actuators: Fundamentals and Applications* (Topics in Mining, Metallurgy and Materials Engineering series, Springer, 2019); https://www.springer.com/gp/book/9783662575321.
42. H. H. Hariri *et al.*, in *2016 IEEE International Conference on Robotics and Automation (ICRA)* (IEEE, 2016), pp. 4743–4749.
43. A. G. Dharmawan, H. H. Hariri, S. Foong, G. S. Soh, K. L. Wood, in *2017 IEEE International Conference on Robotics and Automation (ICRA)* (IEEE, 2017), pp. 6008–6013.
44. A. T. Baisch, O. Ozcan, B. Goldberg, D. Ithier, R. J. Wood, *Int. J. Robot. Res.* **33**, 1063–1082 (2014).

ACKNOWLEDGMENTS

SUPPLEMENTARY MATERIALS

Science

Form and function all in one

Piezoelectric actuators are one route to driving motion in robotic systems. However, one typically needs either multiple crystals or engineered structures to allow motion with multiple degrees of freedom. Cui *et al.* designed architected materials composed of conductive and piezoelectric materials that couple electric field and mechanical strain (see the Perspective by Rafsanjani). The authors were able to engineer these three-dimensional materials to be capable of a variety of motions and transducer functions by using additive manufacturing to build the complex shapes. They demonstrate their functionality for actuation and sensing in a unified miniaturized mobile robot that can move, sense, and perform feedback control. —MSL

View the article online
https://www.science.org/doi/10.1126/science.abn0090
Permissions
https://www.science.org/help/reprints-and-permissions

Use of this article is subject to the Terms of service